On Lagrangian properties of turbulent Rayleigh-Bénard convection – Supplemental material

Stephan Weiss[1], Daniel Schanz[1], Ahmed Oguzhan Erdogdu[1], Andreas Schröder[1,2] and Johannes Bosbach[1]

[1]Department of Experimental Methods, Institute of Aerodynamics and Flow Technology, German Aerospace Center (DLR), Göttingen, Germany
[2]Brandenburgisch Technische Universität (BTU), Cottbus-Senftenberg, Germany

In this supplemental material, we provide additional detailed information that might be of interest for the reader but that in our opinion does not fit into the main text.

1. Lagrangian auto-correlation function

We have presented in fig. 7 the Lagrangian velocity autocorrelation function $C_{uu}(\tau)$, which was calculated over all particle tracks of sufficient length. For homogeneous isotropic turbulence, C_{uu} decreases nearly exponentially over the Lagrangian integral time scale

$$T_L = \int_0^\infty C_{uu}(\tau) d\tau, \tag{1.1}$$

which is assumed to be proportional to its Eulerian equivalent T_E. However, RBC is not homogeneous and also not isotropic on sufficiently large scales. In particular, the inhomogeneity of the system is clearly shown in the vertical velocity profiles (fig. 3 and 4) and therefore, the Lagrangian statistics depend on the initial position of a particle. Furthermore, while RBC is statistically steady, in our experiments the slow dynamics of the large scale flow structure together with a finite measurement time, make the measurements often time-dependent.

For an inhomogeneous turbulent system, the Lagrangian mean velocities depend on the initial position of $\boldsymbol{x}_0$ as well ass the time lag τ and is calculated (see e.g., Monin & Yaglom (1971); Di Bernardino *et al.* (2020)) as

$$\boldsymbol{U}(\boldsymbol{x}_0, \tau) = \frac{1}{N_{\boldsymbol{x}_0}} \sum_{k|x_0} \boldsymbol{u}_L(\boldsymbol{x}_0, \tau), \tag{1.2}$$

with $\boldsymbol{u}_L(\boldsymbol{x}_0, \tau)$ being the Lagrangian velocity of a particle at time τ that has been at $\boldsymbol{x}_0$ at time $\tau = 0$. Here the summation is conducted over all particles that had an initial position $\boldsymbol{x}_0$. In order to calculate $\boldsymbol{U}$ we have binned all positions $\boldsymbol{x}_0$ into a 100x100x40 large grid. Figure 1 shows results calculated for data set SQR16_1 ($Ra = 1.1 \times 10^6$, Pr=7.0, $\Gamma = 16$).

The top row of fig. 1(a,b,c) shows 2d-colormaps of the three velocity components (U, V, W at midheight ($z/H = 0.5$) and $\tau = 0$, i.e., which is equivalent to the averaged Eulerian velocity at this positions. As is seen, the averaged velocities (averaged over $2000\, t_f$) do not sum up to zero and a large scale pattern, which

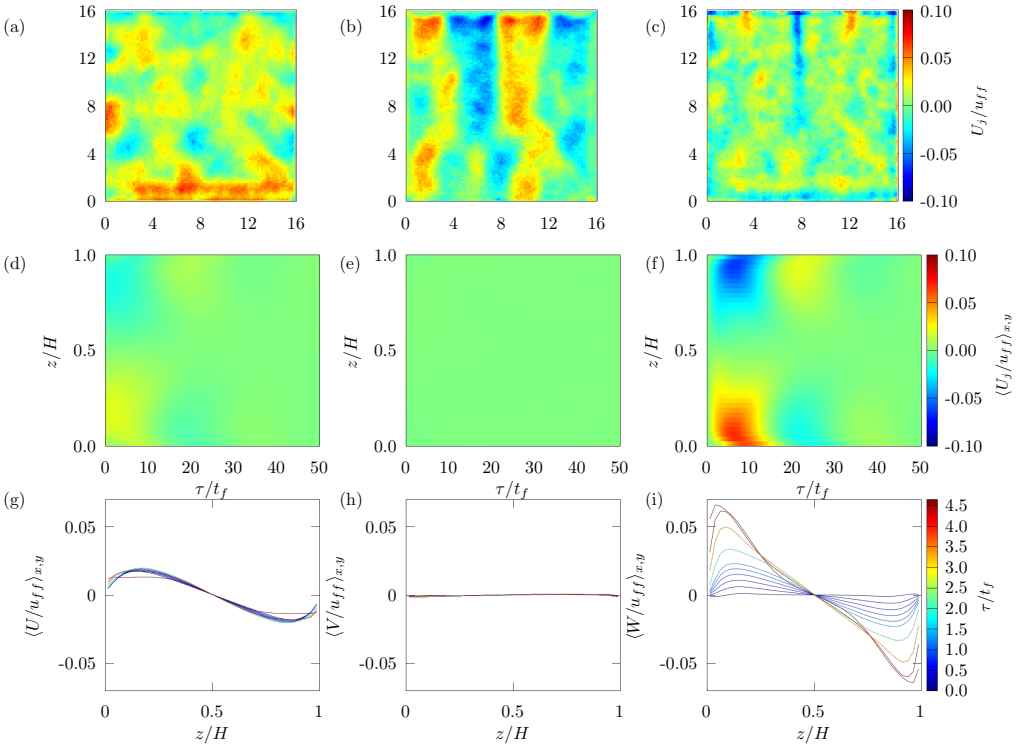

Figure 1: Top: Averaged velocity U (a), V (b), W (c) at midheight for $\tau = 0$. Middle: Space-time plots of the horizontally averaged velocity $\langle U\rangle$ (d), $\langle V\rangle$ (e),$\langle W\rangle$ (f) as function of z . Bottom: Velocity $\langle U\rangle$ (g), $\langle V\rangle$ (h),$\langle W\rangle$ (i) averaged over the horizontal domain as function of z for various τ/t_f (color). The data set for this analysis was SQR16_1 ($Ra = 1.1 \times 10^6$, $Pr = 7.0$, $\Gamma = 16$.)

is aligned in y-direction is clearly visible. This is most likely due to a symmetry breaking due to the cooling flow as discussed previously in Weiss *et al.* (2023).

Intrinsically the symmetry is broken in z-direction, in particular close to the top and bottom plates, and that is where the largest inhomogeneities are expected. Therefore, we now average the velocities over the entire plane and plot in the second row of fig. 1(d, e, f) colormaps representing $\langle U_j\rangle_{x,y}(z_0, \tau)$. For clarity, we also plot profiles for the smallest time intervals ($\tau/t_f \leqslant 4.5$) below in fig. 1(g,h,i).

Let's first have a quick look at the horizontal components. The profiles for $\langle V\rangle_{x,y}$ are very flat and close to zero after horizontal averaging which indicates that this component does not depend on z at least not in the statistical average. On the other hand $\langle U\rangle_{x,y}$ shows a small maximum close to the bottom plate and a small minimum at the top. This is due to a small large scale mean shear flow where warm fluid flows along the bottom plate in positive x-direction and cold flows a long the bottom plate in negative x-direction. As this direction is the same as the flow of our cooling water, we believe that a small temperature gradient in the top plate induces this large scale flow.

The strongest asymmetry between the bottom and the top is shown in $\langle W\rangle_{x,y}$. For small τ there is a clear maximum at the bottom and a minimum at the top. With increasing τ this maximum (minimum) increases (decreases) until around

τ/t_f and decreases afterwards. As can be seen in fig. 1(f) the amplitude of these oscillations decay just after a few oscillations and are not visible anymore after about $50\,t_f$. These oscillations are due to particles that move up and down. Particles that are initially close to the bottom, are most likely after very short time somewhere close to the cell center, where the largest vertical velocities occur (see fig. 3 and 4 in the main text). If they have been close to the bottom (top) at $\tau = 0$, they are likely in an updraft (downdraft) region with large positive (negative) velocity. Clearly after about $20\,t_f$ many particles that have started at the bottom (top) have reached the top and are again on their way down (up) hence the Lagrangian mean velocity becomes negative (fig. 1f).

With the knowledge of the Lagrangian mean velocity, one can now define a velocity standard deviation which again depends on the initial location as well as the time lag:

$$\sigma_j^L(\boldsymbol{x}_0,\tau) = \sqrt{\frac{1}{N_{\boldsymbol{x}_0}}\sum_{k|x_0}\left[u_j^{(k)}(\boldsymbol{x}_0,\tau) - U_j(\boldsymbol{x}_0,\tau)\right]^2}. \tag{1.3}$$

Figure 2 shows very similar plots as fig. 1, just for the standard deviation $\sigma_z^L(\boldsymbol{x}_0,\tau)$. For $\tau = 0$ the standard deviation (fig. 2a,b,c) exhibits similar large scale pattern then the averaged velocities in fig. 1, which indicates that fluctuation intensities correlate with velocity amplitudes. This is somehow expected in a turbulent flow. The same can be deducted from the horizontally averaged vertical profiles in fig. 2(d-i). Fluctuations of the horizontal velocities (σ_x^L and σ_y^L) are for small τ large at the top and the bottom, a fact that is expected already from the vertical profiles of the squared horizontal velocities in fig. 3 and 4 of our main paper. With rising τ the maxima at the top and bottom increase until about $\tau/t_f \approx 5$ and falls off afterwards. Also here, these maxima regrow slightly afterwards but decay very quickly as particle quickly loose memory of their initial starting location.

The vertical component is slightly different. For very small τ a maximum first appears at midheight, which shrinks very quickly with increasing τ and maxima appear close to the top and bottom (fig. 2f and i). The initial maxima in midheight is explained because particle that are at midheight have in general the largest vertical velocity (fig. 3 and 4 in the main text) and therefore it is expected that they also experienced the largest fluctuations. However, after a while particles from the bottom or the top have reached the midheight regions with large fluctuations and therefore maxima occur close to the top and the bottom.

Further, the Lagrangian auto correlation function can be calculated as

$$\rho_j^L(\boldsymbol{x}_0,\tau) = \frac{1}{N_{x_0}}\frac{\sum_{k|x_0}\left\{\left[u_j^{(k)}(\boldsymbol{x}_0,\tau) - U_j(\boldsymbol{x}_0,\tau)\right]\left[u_j^{(k)}(\boldsymbol{x}_0,0) - U_j(\boldsymbol{x}_0,0)\right]\right\}}{\sigma_j^L(\boldsymbol{x}_0,\tau)\sigma_j^L(\boldsymbol{x}_0,0)}. \tag{1.4}$$

Horizontally averaged vertical profiles for the three velocity components are plotted in fig. 3(d,e,f), whereas the same information for large τ can be seen as space-time color plots in fig. 3(a,b,c). We see immediately that again the two horizontal components look the same, while the vertical component is qualitatively different. Therefore, lets quickly have a look at the horizontal component. At small τ, correlation is large close to the top and bottom plates, whereas a

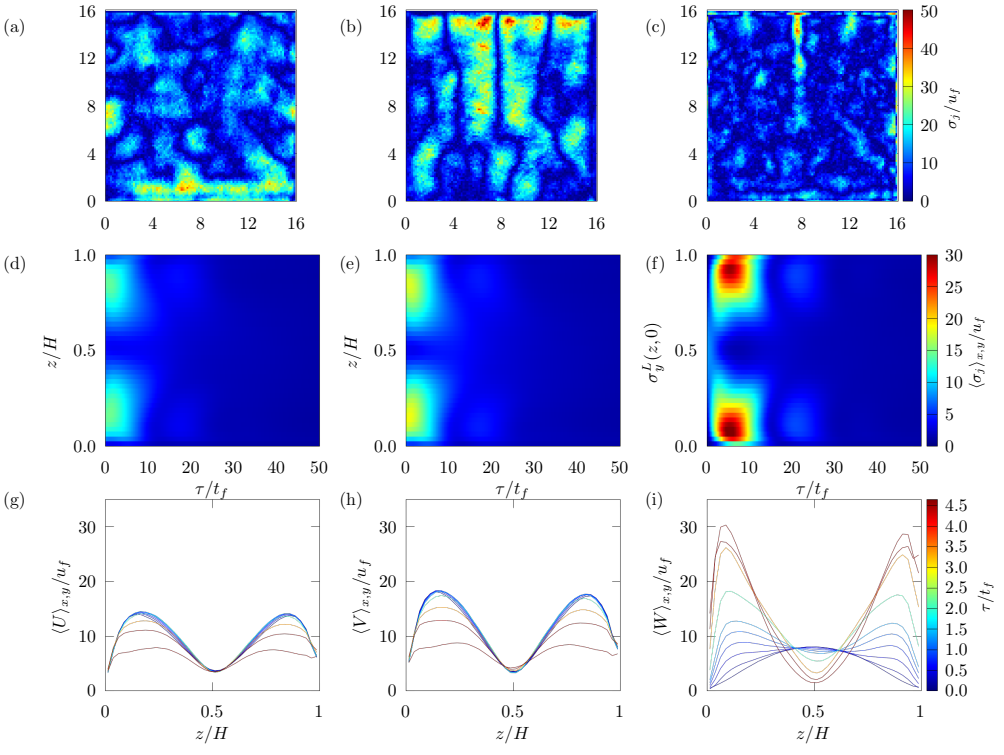

Figure 2: Same as fig. 1 but for different components of σ_j.

minimum develops quickly with increasing τ. Particles that start close to the cell center will soon reach regions of very large fluctuations as shown in fig. 2(d,e,f) which quickly causes the particle velocity to decorrelate. This is in particular the case for particles that are neither in a strong updraft nor a downdraft region but somewhere in between, where buoyancy does not play a big role and the small scale fluctuations are caused by inertial effects.

Particles that are initially close to the top and bottom plate, are more influenced by the large scale eddies of size similar to the cell height H. Therefore, they move along these large convection rolls from the top to the bottom and back, while always changing sign of their horizontal velocities close to the boundaries. This creates the fluctuations shown here in fig. 3(a and b) and in fig. 7 in the main text, which also decay exponentially after sufficient time.

The vertical component $\langle\rho_z^L\rangle(x,y)$ shown in fig. 3(c and f) look inverted to the horizontal components and show for small τ a correlation maximum at the cell center which decays towards the top and bottom. The maximum is because particles close to the cell center are dragged by up- or downdraft and keep their velocity until these particles reach the top or bottom. After that they move in the opposite directions, hence the maximum at the cell center turns into a minimum at around $\tau/t_f \approx 4.5$. The correlation is lost quickly after just one oscillation or so.

Considering the regions close to the top and bottom plates, at small τ the correlation is very small (green in fig. 3c) and tends to zero the closer the particles initial position z_0 is located to the vertical boundaries. This is because particles

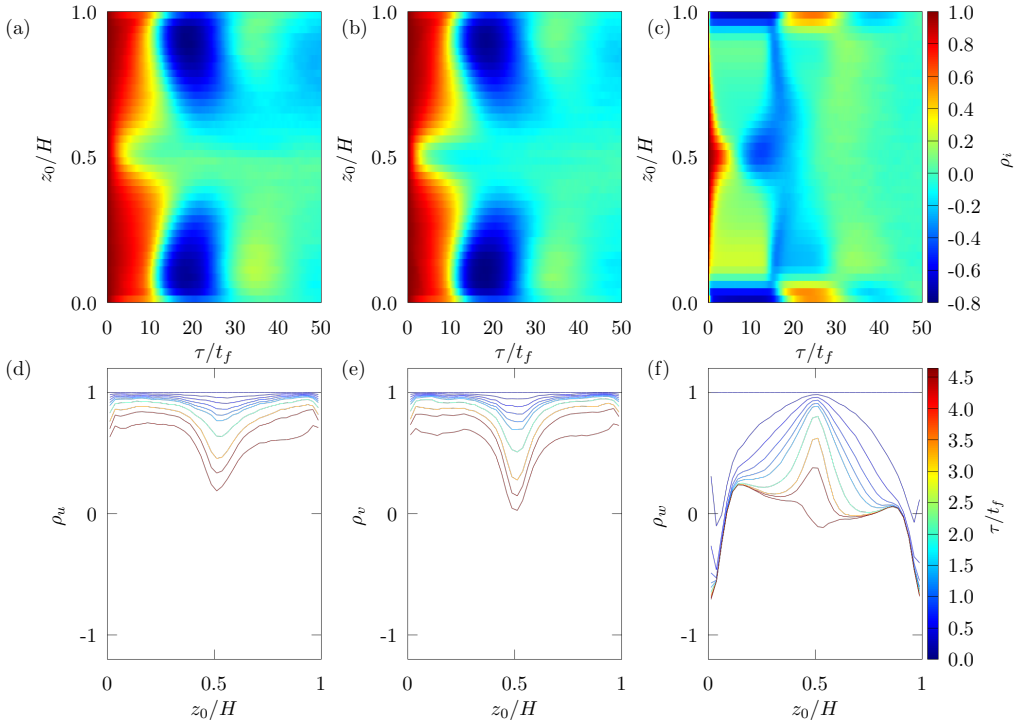

Figure 3: Top row: Space-time plots of the horizontally averaged Lagrangian auto correlation function $\langle \rho_j^L \rangle_{x,y}$ (color) as function of time and vertical position z_0 for the x- (a), the y- (b) and the z- components (c). Bottom row: Representative profiles of small time lags τ (color).

in these regions either keep their velocity causing positive correlation if they at $\tau = 0$ move away from the boundaries, or change direction when they move towards the boundaries, causing negative correlation. Both effects compensate each other causing the correlation to be small. With this explanation, the question remains, why do minima occur close to the top and bottom at small τ? One would expect that close to the bottom, the same number of particles at any given time move towards the boundary and away from it? We believe that the numbers of particles that move towards the plate and away from it is indeed the same, but due to buoyancy close to the plate particles are always accelerated away from the plate. Particles that are very close to the bottom and move downward will very soon experience large acceleration in z-direction that will very quickly change the sign of its vertical components, while inertial effects close to the wall are small. A particle at the same position moving away from the plate will instead decorrelate due to the turbulence in the bulk. Both effects do not cancel out each other.

2. Displacements in anisotropic systems

In sec. 3.4 of the main text, we have analysed the dispersion of single particles

$$\Delta_i^2(\tau) = \langle [x_i(t+\tau) - x_i]^2 \rangle_{t,p}. \tag{2.1}$$

We have also noted already that under the presence of a mean flow a corrected version of the displacement can be written (see Monin & Yaglom (1975)) as:

$$\Delta^2_{c,i}(\tau) = \langle [x_i(t+\tau) - x_i(t) - u_i(t)\tau]^2 \rangle_{t,p}. \tag{2.2}$$

$\Delta^2_{c,i}$ is now not anymore the particle displacement but rather the relative displacement of the particle compared to a position it would had under constant velocity. One can quickly see (adapted from Ouellette (2006)) that $\Delta^2_{c,i}$ is related to the velocity increments $\delta u_i(t,\tau) = u_i(t+\tau) - u_i(t)$:

$$\Delta^2_{c,i}(\tau) = \langle \left[\int_0^\tau \delta u_i(t,t')dt' \right]^2 \rangle_{t,p} \tag{2.3}$$

$$= \int_0^\tau dt' \int_0^\tau dt'' \langle \delta u_i(t,t') \delta u_i(t,t'') \rangle_{t,p}. \tag{2.4}$$

Further, one can write

$$\langle \delta u_i(t,t') \delta u_i(t,t'') \rangle_t = \frac{1}{2}[S_i^2(t') + S_i^2(t'') - S_i^2(|t'-t''|)], \tag{2.5}$$

with

$$S_i^2(\tau) = \langle \delta u_i(t,\tau) \delta u_i(t,\tau) \rangle_t \tag{2.6}$$

being the Lagrangian second order velocity structure function, which is discussed in sec. 3.5 of the main text. Considering that

$$S_i^2(\tau) = a_0 \varepsilon^{3/2} \nu^{-1/2} \tau^2 \qquad \text{for} \quad \tau \ll \tau_\eta, \tag{2.7}$$

$$S_i^2(\tau) = C_0 \varepsilon \tau \qquad \text{for} \quad \tau_\eta \ll \tau \ll T_0, \tag{2.8}$$

$$S_i^2(\tau) = 2\langle u_i^2 \rangle \qquad \text{for} \quad T_0 \ll \tau, \tag{2.9}$$

one can integrate eq. 2.4 and derive the following relations:

$$\Delta^2_{c,i}(\tau) = \frac{5}{24} a_0 \varepsilon^{3/2} \nu^{-1/2} \tau^4 \qquad \text{for} \quad \tau \ll \tau_\eta, \tag{2.10}$$

$$\Delta^2_{c,i}(\tau) = \frac{1}{3} C_0 \varepsilon \tau^3 \qquad \text{for} \quad \tau_\eta \ll \tau \ll T_0, \tag{2.11}$$

$$\Delta^2_{c,i}(\tau) = \langle u_i^2 \rangle \tau^2 \qquad \text{for} \quad T_0 \ll \tau. \tag{2.12}$$

Analyses of two representative data sets are shown in fig. 4. There, we have plotted $\Delta^2_{c,i}/H^2$ (fig. 4 a and c) and also for better visibility the same data compensated by $(\tau/t_f)^2$ (b and d). Lets first have a look at fig. 4(a and b) which shows data for a rather small $Ra = 1.1 \times 10^6$ and large $Pr = 7.0$, hence the flow is not very turbulent and the energy injection scale is not well separated from the viscous scales. The three components $\Delta^2_{x,c}$, $\Delta^2_{y,c}$ and $\Delta^2_{z,c}$ overlap decently well, with $\Delta^2_{c,z}$ exhibiting slightly larger values than the two horizontal components, an observation we have seen and discussed already for the Lagrangian structure function in sec. 3.5 of the main paper.

For large $(\tau/t_f) > \tau_{co}$ the data are well represented by eq. 2.12, which shows that correlation is lost and particles disperse diffusively. For very small $\tau \lesssim 10$ their slope is clearly steeper and seems to be indeed well represented by eq. 2.10. On intermediate time scales the data do need seem to exhibit a very clear power law scaling but rather show a more continuous change of the slope in the log-

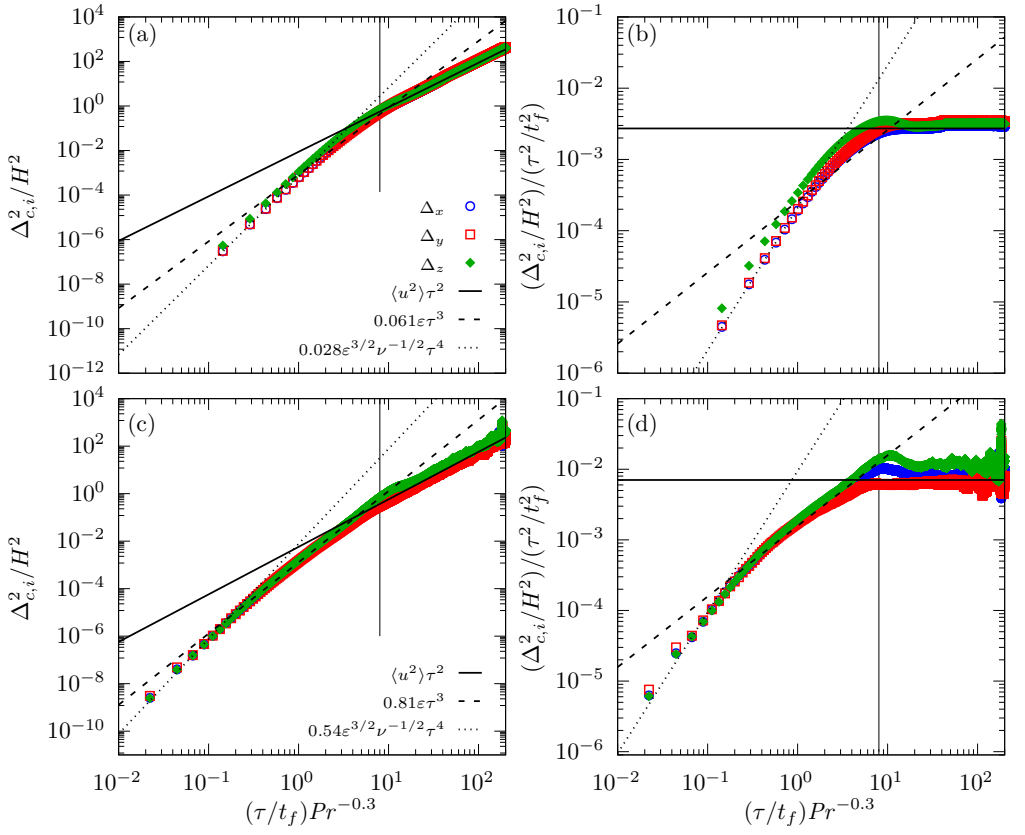

Figure 4: Displacement according to eq. 2.2 (a and c) as well as the displacement compensated τ^2 (b and d) for two different datasets SQR16_1 ($\Gamma = 16$, $Ra = 1.1 \times 10^6$, $Pr = 7.0$ a and b) and for CYL1_3 ($\Gamma = 1$, $Ra = 1.53 \times 10^9$, $Pr = 0.7$, b and d). The vertical black line marks $\tau/t_f = \tau_{co}$ as a guide to the eyes. The dashed and dotted black lines mark fits of eq. 2.11 and 2.10 to the data. The solid black line marks $\langle u^2\rangle\tau^2$.

log representation, which is most likely due to the low turbulence intensity and insufficient scale separation.

Hence, we also analyse in fig. 4(c and d) data from a much more turbulent case (dataset CYL1_3) Also here, for $\tau > \tau_{co}$ a clear regime with $\Delta_{c,i} = \langle u^2\rangle\tau^2$ is observed as well as a viscosity dominated regime ($\propto \tau^4$) for very small τ. Now, here we find an intermediate regime with a rather constant power law scaling, which can be well approximated by $\propto \tau^3$. We note that also here the transition to the $\propto \tau^2$ regime is nearly the same for the two very different datasets when scaled by $Pr^{0.3}$, i.e., $\tau_{co} Pr^{-0.3} \approx 8$.

3. Horizontal anisotropy of the second order velocity structure function

In sec. 3.5. in the paper, we present (fig. 10) and discuss the second order Lagrangian velocity structure function $S_i^2(\tau)$ for two representative data sets. For the highly turbulent data set CYL1_3 with $Ra = 1.5 \times 10^9$, we observe a scaling

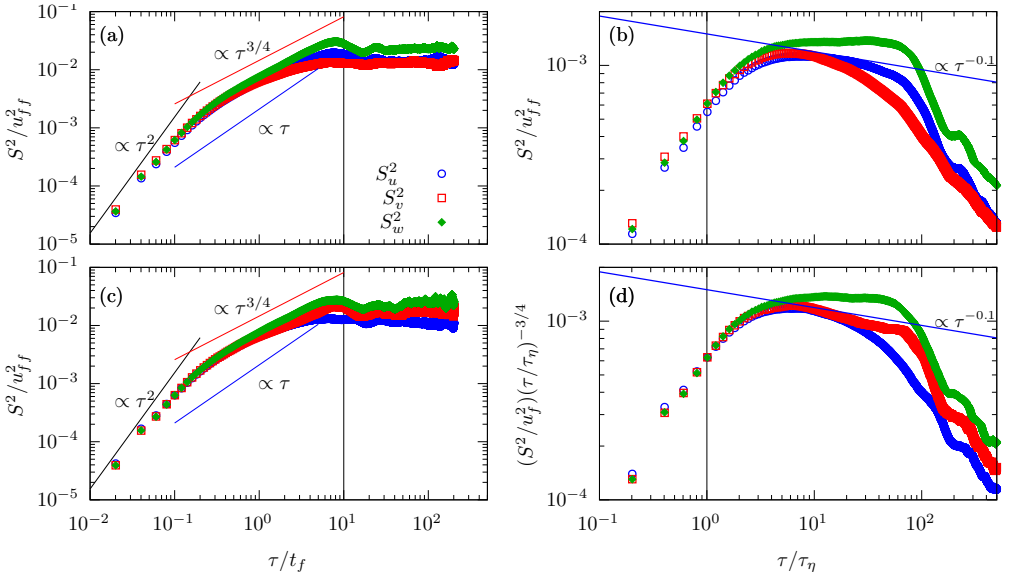

Figure 5: Lagrangian velocity structure function for dataset CYL1_3 ($Ra = 1.5 \times 10^9$, Pr=0.7, $\Gamma = 1$). (a and b): Evaluated in a fixed coordinate system. (c and d): Evaluated in a co-rotating coordinate system given by the orientation of the LSC. (a and c): Data plotted against time, normalised by the free-fall time t_f. (b and d): Time is here normalised by the Kolmogorov time scale τ_η.

for the vertical component $S_w^2 \propto \tau^{3/4}$ but different data for the two horizontal components. While $S_u^2 \propto \tau^{0.65}$, no clear power law was observed for S_v^2. We have attributed this difference in the two horizontal components with the large scale circulation roll (LSC). In order to find more evidence for this claim, we have calculated the orientation of the LSC at a given time step as sum of the angular momentum of all particles, i.e.,

$$\boldsymbol{L} = \sum_i \boldsymbol{r}_i \times \boldsymbol{v}_i.$$

The angle of the LSC is then given by its horizontal component, i.e., $\theta = arg(L_x + iL_y)$. Having calculated θ for every time step, we now rotate our coordinate system so that new x-axis is always parallel to (L_x, L_y) and the y-axis perpendicular to it.

The results are shown in fig. 5(c and d). For comparison we show in fig. 5(a and b) $S_i^2(\tau)$ as measured in the laboratory frame. The difference becomes apparent when comparing fig. 5(b) and (d). In (d) now the red squares S_v^2 show a scaling behaviour $\propto S^{0.65}$, whereas the blue circles (S_u^2) decreases much earlier. This observation is evidence that indeed the difference in the two horizontal components is caused by orientation of the LSC.

REFERENCES

Di Bernardino, Annalisa, Monti, Paolo, Leuzzi, Giovanni & Querzoli, Giorgio 2020 Eulerian and Lagrangian time scales of the turbulence above staggered arrays of cubical obstacles. *Environmental Fluid Mechanics* **20**, 987.

Monin, A. S. & Yaglom, A. M. 1971 *Statistical Fluid Mechanics: Mechanics of Turbulence, vol. 1*. Cambridge, Massachusetts: The MIT Press.

Monin, A. S. & Yaglom, A. M. 1975 *Statistical Fluid Mechanics: Mechanics of Turbulence, vol. 2*. Cambridge, Massachusetts: The MIT Press.

Ouellette, Nicholas Testroet 2006 Probing the statistical structure of turbulence with measurements of tracer particle tracks. PhD thesis, Cornell University.

Weiss, Stephan, Schanz, Daniel, Erdogdu, Ahmed Oguzhan, Schröder, Andreas & Bosbach, Johannes 2023 Investigation of turbulent superstructures in Rayleigh-Bénard convection by Lagrangian particle tracking of fluorescent microsphers. *Exp. Fluids* **64**, 82.